

Coexisting Paramagnetic Spins and Long-Range Magnetic Order in $\text{Ba}_4(\text{Ru}_{0.92}\text{Ir}_{0.08})_3\text{O}_{10}$

Farhan Islam,¹ Jiasen Guo,¹ Wei Tian,¹ Bing Li,¹ Xudong Huai,²
Thao T. Tran,² Gang Cao,³ Zachary Morgan,¹ and Feng Ye^{1,*}

¹*Neutron Scattering Division, Oak Ridge National Laboratory, Oak Ridge, Tennessee 37831, USA*

²*Department of Chemistry, Clemson University, Clemson, South Carolina 29634, USA*

³*Department of Physics, University of Colorado at Boulder, Boulder, Colorado 80309, USA*

(Dated: March 9, 2026)

We investigate the effect of dilute Ir substitution on the magnetism of the trimer-based ruthenate $\text{Ba}_4\text{Ru}_3\text{O}_{10}$ using neutron diffraction, magnetic susceptibility measurements, atomistic simulations, and first-principles calculations. Neutron diffraction shows that Ir doping preserves the zigzag antiferromagnetic structure and the ordered-moment magnitude of the parent compound, in which the moments reside exclusively on the two outer Ru(2) sites of each Ru_3O_{12} trimer, while the central Ru(1) site remains nonmagnetic. The Néel temperature is reduced from ≈ 105 K to $84.0(1)$ K upon 8% Ir substitution, while magnetic susceptibility reveals a pronounced low-temperature Curie-like upturn, indicating the coexistence of paramagnetic spins with long-range antiferromagnetic order. Density-functional calculations shows that Ir preferentially occupies the central Ru(1) site, where its extended $5d$ orbitals disrupt the Ru–Ru molecular-orbital network and intra/inter-trimer exchange pathways. Atomistic simulations incorporating this paramagnetic dilution reproduce the suppressed ordering temperature and the coexistence of ordered and paramagnetic components.

I. INTRODUCTION

The structural diversity of ruthenium-based oxides has made them a central platform for exploring emergent electronic and magnetic behavior in correlated $4d$ materials [1–7]. Depending on the RuO_6 octahedra connectivity, ruthenates span a wide range of physical regimes: layered compounds with corner-sharing octahedra such as Sr_2RuO_4 support unconventional superconductivity [6, 7], while other members of the family incorporate face-sharing or edge-sharing octahedra that assemble into dimers, trimers, or larger cluster units [8–12]. These cluster-based materials are particularly intriguing because the shortened metal–metal distances within face-sharing units promote Ru–Ru overlap, enabling the formation of molecular-orbital-like electronic states that compete with conventional crystal-field-split ionic configurations. This internal electronic differentiation can modify the magnetic exchange pathways, producing anisotropic interactions, quasi-one-dimensional behavior, or unusual temperature-dependent crossovers between localized and itinerant regimes [13–18].

In face-sharing ruthenates, the magnetic behavior is influenced by the cardinality and internal structure of the Ru–O cluster units. In dimer-based systems, inter-site d – d hopping within face-shared RuO_6 pairs can promote the formation of covalent molecular orbitals, partially excluding electrons from the magnetic subsystem and suppressing the effective moment [19]. When local moments persist on the dimers, the magnetic ground state is controlled by the competition between strong intradimer exchange and inter-dimer coupling, with long-

range order emerging when the two energy scales become comparable [20–25]. Trimer-based face-sharing ruthenates introduce additional internal degrees of freedom associated with three coupled Ru ions, leading to a richer internal organization of electronic and magnetic charac-

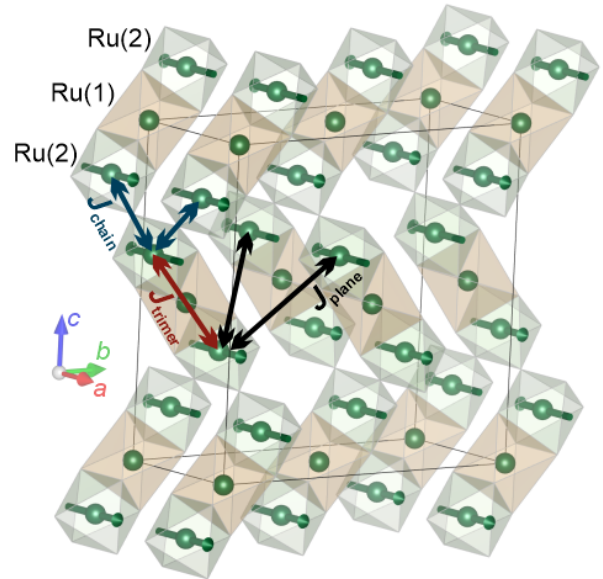


FIG. 1. Magnetic structure of parent and Ir-doped $\text{Ba}_4\text{Ru}_3\text{O}_{10}$, showing the three-dimensional network of face-sharing RuO_6 octahedra; oxygen and barium atoms omitted for clarity. The face-sharing geometry forms Ru_3O_{12} trimers composed of a central Ru(1) ion and two outer Ru(2) ions. The arrows illustrate the dominant magnetic exchange pathways: the intra-trimer coupling J_{trimer} (red), the inter-trimer chain coupling J_{chain} (blue), and the in-plane inter-trimer coupling J_{plane} (black).

* Contact author: yefl@ornl.gov

ter among the Ru sites within the cluster [26, 27]. In addition to this internal trimer physics, it is naturally expected that the connectivity between Ru_3O_{12} trimers also plays an important role in determining the magnetic behavior, as it sets the pathways through which magnetic interactions propagate between clusters. For example, in lanthanide-containing trimer ruthenates, linkage through intervening LnO_6 octahedra modifies the magnetic response [28]. More generally, these observations emphasize that both the delocalized electronic configuration of Ru_3O_{12} trimers and their inter-trimer connectivity need to be considered to understand the complex magnetic responses in this class of materials.

$\text{Ba}_4\text{Ru}_3\text{O}_{10}$ (BRO) provides a particularly well-defined platform for investigating magnetism in cluster-based $4d$ systems. BRO adopts a simple orthorhombic structure composed of face-sharing RuO_6 octahedra forming Ru_3O_{12} trimers, which are further connected through corner-sharing pathways and support three-dimensional antiferromagnetic long-range order [Fig. 1]. Magnetically, BRO is intrinsically unconventional: only the outer Ru(2) sites develop ordered moments, while the central Ru(1) site remains nonmagnetic, revealing site-selective magnetism associated with the trimer-based electronic structure [13–15].

The suppression of magnetic moment at the Ru(1) site was rationalized through different theoretical proposals. First, it was proposed to originate from the strong Ru(1) O_6 octahedral distortion, which lifts the t_{2g} degeneracy and produces a large internal splitting (~ 0.4 eV). The four d -electrons occupy the two lowest t_{2g} levels, leading to a nonmagnetic configuration at Ru(1). In contrast, the Ru(2) octahedron is less distorted, producing only weak t_{2g} splitting (~ 0.15 eV), allowing Hund’s exchange to stabilize an $S = 1$ state with a $\sim 2 \mu_B$ moment [15]. Alternatively, the combination of molecular-orbital (MO) framework and charge redistribution developed in Refs. [14, 26] provides an explanation for the site-selective magnetism in BRO. In a face-sharing Ru_3O_{12} trimer, the three Ru a_{1g} orbitals form bonding (B), nonbonding (NB), and antibonding (AB) molecular orbitals. The central Ru(1) ion only participates in the B and NB molecular orbital and the corresponding a_{1g} states are pushed away from the Fermi level, while the NB molecular orbital involves the two outermost Ru(2) sites and forms a well defined density of states peak at the Fermi energy. In addition, Ru(1) has more $4d$ electrons due to the longer Ru–O bond lengths [13]. Such charge disproportionation is confirmed by the General Gradient Approximation (GGA) calculation [26]. This creates weaker Ru–O hybridization and further lowers the on-site $4d$ energy (remove the Ru(1) weight from the Fermi level). As the combined result, the lack of density of states $N(E_F)$ for Ru(1) renders the site nonmagnetic due to the Stoner criteria $IN(E_F) \sim 0$, where I is the Stoner electron-electron exchange parameters [29].

The presence of long-range AFM order in BRO despite a magnetically silent Ru(1) site indicates that mag-

netic order is sustained by a finely tuned network of exchange interactions. This is reflected in the critical behavior: the order-parameter exponent β is close to that of a three-dimensional Heisenberg system, while the spin dynamics remain strongly anisotropic, as evidenced by a sizable spin-wave gap [15]. Such features suggest that the magnetic ground state is susceptible to perturbations that modify local exchange pathways. Our neutron diffraction measurements show that the Ir-substituted system retains the same commensurate propagation vector, $\mathbf{k} = (0, 0, 0)$, and zigzag AFM structure as the parent compound, while the Néel temperature is suppressed to $T_N = 84(1)$ K. As in the parent material, the ordered moments reside exclusively on the outer Ru(2) sites, whereas magnetic susceptibility reveals a low-temperature Curie-like contribution indicative of paramagnetic moments introduced by Ir substitution. Monte Carlo and Landau–Lifshitz–Gilbert simulations support this interpretation, showing that Ir dilution locally disrupts exchange interactions and suppresses T_N without altering the underlying trimer-based magnetic topology.

II. EXPERIMENTAL DETAILS

Single crystals of $\text{Ba}_4(\text{Ru}_{1-x}\text{Ir}_x)_3\text{O}_{10}$ were grown using a high-temperature flux method following the procedure described in Ref. [30]. Off-stoichiometric mixtures of RuO_2 , BaCO_3 , and BaCl_2 flux were combined. For the Ir-substituted samples, IrO_2 was introduced in place of a corresponding fraction of RuO_2 to achieve the desired nominal doping level. The mixed powders were thoroughly ground, loaded into platinum crucibles, and heated to ensure complete melting. The melts were then slowly cooled to room temperature to promote single-crystal formation. Energy-dispersive X-ray (EDX) spectroscopy was used to verify the chemical composition of the crystals, confirming an Ir concentration of $\text{Ba}_4(\text{Ru}_{0.92}\text{Ir}_{0.08})_3\text{O}_{10}$ within experimental uncertainty.

The structure information was investigated at ORNL using a Rigaku Synergy-DW diffractometer equipped with a HyPix-Arc 150° detector. A rotating molybdenum anode was used to generate X-rays with wavelength $\lambda = 0.7107$ Å. The sample temperature was controlled in the range of 90–300 K by a nitrogen gas flow provided by an Oxford cryosystem. The data were collected and reduced using Rigaku CryAlisPro software. Single crystal with dimension of $0.05 \times 0.05 \times 0.02 \text{mm}^3$ was mounted using Paratone-N oil on MiTeGen micro-mount. The crystal was positioned at 50 mm from the detector. Magnetic susceptibility was measured using a Quantum Design Magnetometer (7 T MPMS). Neutron diffraction measurements were performed using the single crystal diffuse scattering spectrometer CORELLI [31] at the Spallation Neutron Source and VERITAS triple axis spectrometer at High Flux Isotope Reactor of Oak Ridge National Laboratory. A single crystal with dimension approximately $1.5 \times 1.5 \times 0.5 \text{mm}^3$ was used.

The sample was glued on an aluminum pin and cooled using a closed-cycle refrigerator, with temperature controlled from 5 to 300 K. The sample was oriented with $[0, 0, L]$ out-of-plane aligned with the primary rotation axis. Three-dimensional reciprocal-space volume data were collected at CORELLI at both 5 K and 120 K by rotating the crystal 360° at 1.5° step. For VERITAS, reflections accessible in the scattering plane are collected for the magnetic structure refinements.

III. RESULTS AND DISCUSSION

The T -dependence of the magnetic susceptibility of parent and Ir-doped BRO are compared in Figs. 2(a)-2(b). For the parent compound, the magnetic susceptibility shows strong anisotropy along three crystallographic axes. $\chi_a(T)$ displays the most pronounced kink at 105 K and subsequent suppression at lower temperature, consistent with a spin easy-axis along the a direction. In the Ir-doped sample, the kink anomaly along a shifts to a lower temperature at 84 K. In addition, a pronounced Curie-like upturn develop for all field orientations at low temperature.

To understand the evolution of the magnetic structure upon Ir-doping, an extensive survey in reciprocal space map was conducted at 5 and 120 K for the Ir-doped BRO [Figs. 3(a)-3(b)]. There is no apparent structural phase transition upon cooling. Bragg reflections can be well indexed using the reported orthorhombic space group $Cmca$ (No. 64) with $a = 5.67(1)$ Å, $b = 13.245(2)$ Å and $c = 13.064(2)$ Å at 5 K [13]. No additional superlattice reflection are observed. However, the peaks at low momentum transfer such as $(1, 1, 0)$, $(1, 3, 0)$ and symmetry equivalent locations show clear enhancement in intensity at low- T , which is confirmed by the line-cut comparison along the $[1, K, 0]$ direction [Fig. 3(c)]. The resolution-limited peak width establishes the formation of long-range magnetic order with a propagation vector $\mathbf{k} = (0, 0, 0)$. The temperature dependence of the integrated $(1, 1, 0)$ peak intensity measured on VERITAS (HB1A) shows the onset of magnetic order at 84(1) K [Fig. 3(d)], matches well with the magnetic susceptibility data.

The commensurate wavevector indicates that the magnetic periodicity is the same as the crystallographic unit cell. Symmetry analysis using MAXMAGN [32–35] identifies eight magnetic space groups (MSGs) that are compatible with the crystal structure. Details of the magnetic structure refinement procedure are provided in Appendix A. Among all models tested, MSG $Cmc'a$, depicted in Fig. 1, provides the best refinement with goodness of fit = 0.89. The magnetic structure preserves the same zigzag AFM configuration as in the parent compound [15], with the ordered moment for Ru(2) is $1.01(6)$ μ_B , and nonmagnetic central Ru(1). It is worth noting that the refined magnetic structure places the ordered moments along the crystallographic a axis, consistent with previous neutron

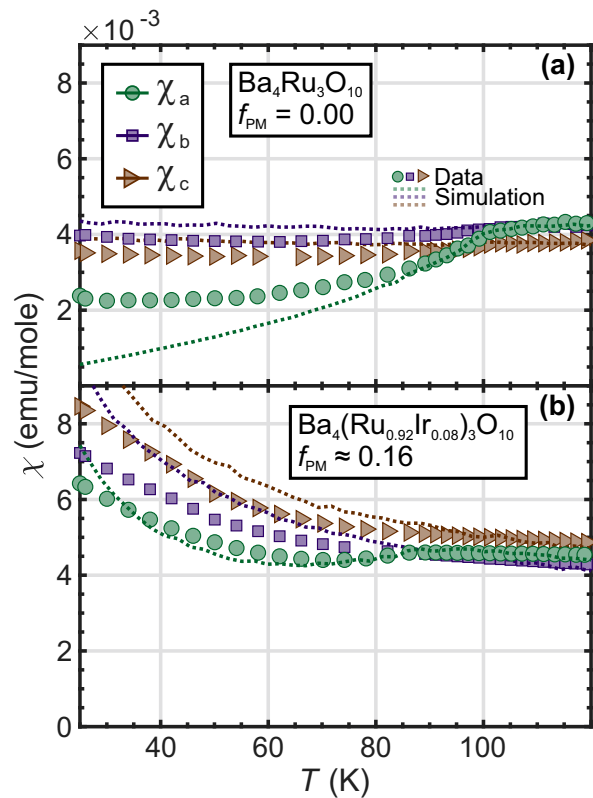


FIG. 2. Temperature-dependent magnetic susceptibility $\chi(T)$ of (a) $\text{Ba}_4\text{Ru}_3\text{O}_{10}$ and (b) $\text{Ba}_4(\text{Ru}_{0.92}\text{Ir}_{0.08})_3\text{O}_{10}$, measured with magnetic fields applied along the three crystallographic axes. The dotted curves are results of Monte Carlo spin-dynamics simulations described in Appendix C. In the parent compound, $\chi_a(T)$ shows a pronounced anomaly at $T_N \approx 105$ K and suppression at lower temperatures, consistent with an easy axis along a . Upon Ir substitution, the anomaly shifts to $T_N \approx 84$ K and a Curie-like upturn develops at low temperature for all field directions, indicating the emergence of weakly coupled paramagnetic spins. In the simulations, Ir substitution is modeled by diluting the exchange network through the removal of exchange bonds associated with a fraction of paramagnetic Ru sites.

diffraction results [13], but contrasts with the c -axis moment direction proposed earlier [13], which lacked access to in-plane magnetic Bragg reflections such as $(1, 1, 0)$.

While neutron diffraction shows that Ir substitution preserves the zigzag AFM ground state, moment size and orientation of the parent compound, bulk magnetic measurements reveal quantitative differences. In particular, the Néel temperature is reduced and the susceptibility develops a Curie-like upturn. These observations indicate that dilute Ir substitution perturbs the magnetic exchange network without altering the overall magnetic topology. To uncover the microscopic origin of the suppressed T_N and the additional paramagnetic response, we combine electronic-structure calculations with atomistic simulations.

Spin-polarized density-functional calculations is per-

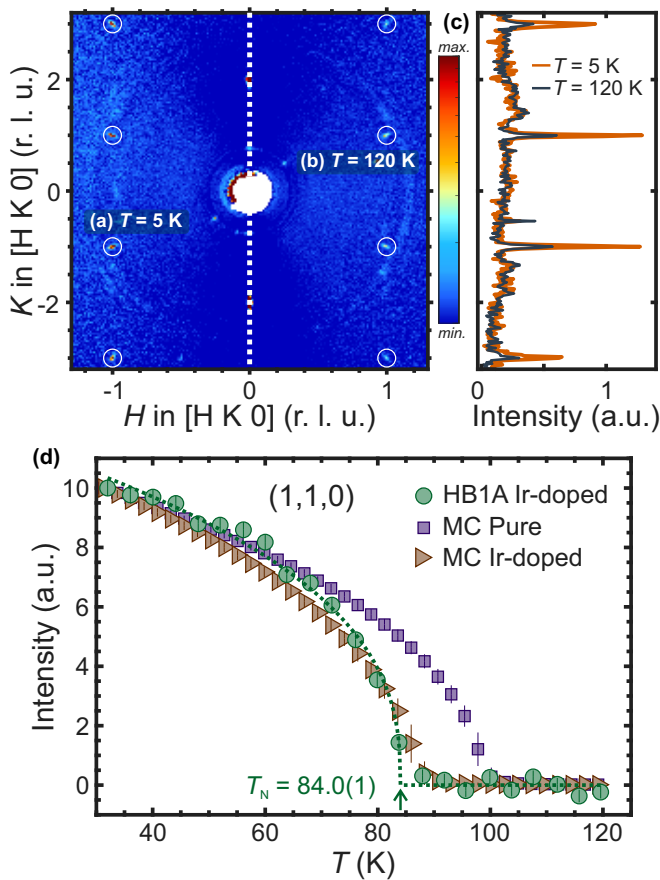


FIG. 3. Neutron diffraction map of Ir-doped $\text{Ba}_4\text{Ru}_3\text{O}_{10}$ in the $(H, K, 0)$ plane at (a) $T = 5$ K and (b) $T = 120$ K, showing enhanced magnetic Bragg peak intensity (circled) at low temperature. (c) Line cuts along the K direction, obtained by integrating over $H \in [0.9, 1.1]$ and $L \in [-0.1, 0.1]$, comparing data at $T = 5$ K and 120 K and highlighting the enhanced magnetic intensity at the $(1, 1, 0)$ and $(1, 2, 0)$ reflections at low temperature. (d) Thermal evolution of the integrated magnetic intensity of the $(1, 1, 0)$ peak measured on VERITAS (HB-1A), fitted to extract Néel temperature $T_N = 84.0(1)$ K. Monte Carlo (MC) spin-dynamics simulations reproduce the ordering temperatures of both the parent compound ($T_N \approx 105$ K) and the Ir-doped sample. In the simulations, Ir substitution is modeled by diluting the exchange network through the introduction of weakly interacting paramagnetic Ru sites.

formed for both the parent and Ir-doped $\text{Ba}_4\text{Ru}_3\text{O}_{10}$ (Appendix B). In the doped case, one of the twelve Ru sites was replaced by Ir, corresponding to an effective substitution level of 8.3%. Three configurations were considered: the undoped structure, Ir substitution at the central Ru(1) site, and Ir substitution at an edge Ru(2) site. Total-energy calculations (Table III) indicate that substitution at the Ru(1) site is energetically favored among the doped cases. Atomic force and stress analysis further reveal enhanced local distortions near the dopant site, consistent with the more spatially extended nature of Ir $5d$ orbitals. Figures 4(a)-4(b) show the spin-density

iso-surface plots of the parent and doped compounds. A large contrast between the middle and edge atoms is evident, underscoring the magnetic distinction between the two Ru sites. The Ru(2) sites exhibit much large spin imbalance comparing to the Ru(1) one, confirming their role as magnetic hosts. The spin density shows no clear asymmetry between the two Ru(2) edge sites, which is consistent with Ir primarily occupying Ru(1). Furthermore, the spin imbalance is negligible at the Ru(1) site in the doped case, revealing that Ir remains magnetically silent. This behavior is consistent with reduced moment in the $5d$ iridates due to enhanced spin-orbit coupling and extended $5d$ orbitals [36].

Based on the preferred Ir substitution sites inferred from the electronic structure calculations, we employed Monte Carlo (MC) and Landau-Lifshitz-Gilbert (LLG) spin-dynamics approaches to determine the magnetic ground state and finite-temperature magnetic response. The LLG calculations were performed using the SUNNY package [37]. Ir substitution occur preferentially at the central Ru(1) site, where it locally disrupts the intratrimer exchange interaction J_{trimer} that couples the two outer Ru(2) ions within a Ru_3O_{12} trimer. The intertrimer exchange interactions J_{chain} and J_{plane} , which connect neighboring trimers along the zigzag chains and within the crystallographic plane, are likewise treated as locally disrupted for the same trimer. As a result, the Ru(2) ions adjacent to an Ir-centered trimer behave as paramagnetic $S = 1$ moments. Ir doping was implemented by introducing a fraction f_{PM} of paramagnetic Ru(2) sites, for which all exchange interactions with neighboring magnetic ions were removed. For 8% Ir substitution, this dilution mechanism corresponds to a paramagnetic Ru-spin concentration of $f_{\text{PM}} \approx 0.16$. Details of the spin Hamiltonian, simulation protocols, exchange parameters, and the implementation of Ir-induced dilu-

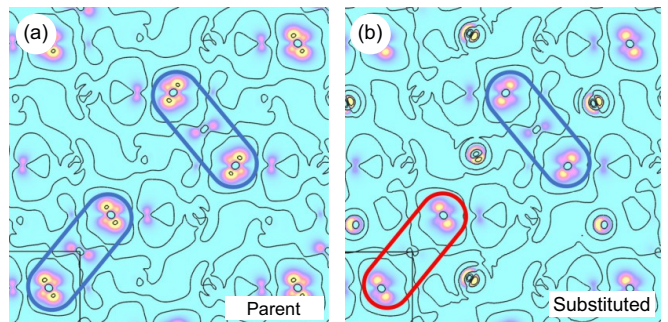


FIG. 4. Spin-density maps for (a) the parent and (b) the Ir-substituted $\text{Ba}_4\text{Ru}_3\text{O}_{10}$ compound. Blue and red elliptical outlines mark the parent and Ir-substituted Ru_3O_{12} trimers, respectively. In the parent system, the spin density is concentrated on the two outer Ru(2) sites of each trimer, while the central Ru(1) site exhibits negligible spin polarization, highlighting the site-selective nature of magnetism. The substituted Ru(1) site shows negligible spin polarization, indicating that Ir remains magnetically silent.

tion are provided in Appendix C.

Using the exchange parameters reported in Ref. [15], the simulations reproduce both the zigzag antiferromagnetic ground state and the temperature dependence of the magnetic intensity in the parent and Ir-substituted compounds [Fig. 3(d)]. The corresponding magnetic susceptibilities obtained from the same models are shown as dotted curves in Fig. 2. The calculations capture the key experimental trends for both compositions, including the suppression of the Néel temperature upon Ir substitution, the reduced low-temperature magnitude of $\chi_a(T)$, and the emergence of a Curie-like upturn associated paramagnetic Ru spins.

Ir represents a particularly strategic substitutional perturbation for this system. According to Shannon's revised ionic radii for octahedral coordination, Ru^{4+} (0.62Å) and Ir^{4+} (0.625Å) possess nearly identical effective ionic sizes [38], implying minimal structural mismatch and preserving the underlying lattice framework upon substitution. In an earlier thermodynamic and transport study, the effects of Ir substitution on the magnetic and electronic properties are investigated for polycrystalline $\text{Ba}_4(\text{Ru}_{1-x}\text{Ir}_x)_3\text{O}_{10}$ ($0.00 \lesssim x \lesssim 0.17$) [39]. The magnetic susceptibility are fit to a dimer model comprised of the interacting Ru(2)–Ru(2) spins, the authors concluded that the main effect of Ir doping is a monotonic reduction in the intra-dimer interaction while the inter-dimer exchange coupling remains unchanged. However, such model only describes the thermodynamics quantity near the transition and fails to explain the apparent upturn in magnetic susceptibility with increasing Ir concentration far below the transition.

On the other hand, the local disruption of exchange interactions due to Ir substitution can be intuitively understood within the molecular-orbital framework. In the presence of trigonal distortion within the face-sharing Ru_3O_{12} trimer, the Ru t_{2g} manifold splits into an a_{1g} orbital oriented along the trimer axis and two e'_g orbitals lying perpendicular to it. In the parent compound, magnetic couplings involve electronic states that are delocalized over the face-sharing Ru_3O_{12} unit [26]. Substituting Ir^{4+} ($5d^5$) at the central Ru(1) $^{4+}$ ($4d^4$) site introduces an electronically distinct ion into this delocalized network by introducing an additional d electron and enhanced spin-orbit coupling. Therefore, the substitution perturbs the hybridization pathways that underpin both intra- and inter-trimer exchange interactions. Consequently, each substituted Ir ion in the Ru(1) site decouples the adjacent two Ru spins. Further studies could clarify whether the effects of Ir substitution arise primarily from the enhanced spin–orbit coupling or from the additional d electron. This question could be addressed through comparative substitutions with ions of similar size, such as Os^{4+} ($5d^4$) and Rh^{4+} ($4d^5$).

Despite the local disruption of magnetic exchange, the preservation of long-range order can be understood from two complementary considerations. First, first-principles calculations for the parent compound show that compet-

ing magnetic configurations are separated by substantial energy scales [26], reversing the relative alignment within a Ru_3O_{12} trimer incurs an energy cost on the order of tens of meV per formula unit, indicating that the zigzag AFM state is energetically favorable against local perturbations. Second, the fraction of Ru sites rendered paramagnetic by Ir substitution ($\sim 16\%$) remains well below the percolation threshold of the three-dimensional exchange network to disrupt the exchange network. Thus, the dilution primarily generates paramagnetic local moments without destabilizing the global magnetic configuration.

Both bond valence sum [14] and first-principles calculations [26] imply that the Ru_3O_{12} trimers in BRO exhibit significant charge disproportionation between crystallographically inequivalent Ru sites (~ 0.52 electron per atom). This redistribution of charge is expected to modify the local electronic potential and magnetic exchange interactions, and it naturally suggests the presence of an incipient charge-density-wave (CDW)–like instability associated with the trimer framework [40]. In cluster-based systems with strong metal–metal hybridization, charge disproportionation can serve as a precursor to long-range charge order correlations that are coupled to lattice and magnetic degrees of freedom. In BRO, this interplay may be central to the emergence of site-selective magnetism and the sensitivity of the magnetic ground state to modest chemical substitution. Despite these indications, direct experimental evidence for static long-range charge order remains elusive, partially because of the small lattice distortions, dynamical or even unconventional charge correlations. Future studies using charge-sensitive probes, such as resonant X-ray scattering will be essential to clarify the nature of the charge correlations in this system.

IV. CONCLUSION

In summary, we have shown that dilute Ir substitution in $\text{Ba}_4\text{Ru}_3\text{O}_{10}$ provides a controlled route to perturb the trimer-based magnetic network without altering the underlying zigzag antiferromagnetic structure. Magnetic susceptibility measurements reveal a reduction of the Néel temperature and the emergence of a Curie-like upturn at low temperatures, indicating the presence of paramagnetic moments introduced by Ir doping. Neutron diffraction establishes that long-range magnetic order persists in the doped compound, with the ordered moments remaining confined to the outer Ru(2) sites and the magnetic structure unchanged from that of the parent compound. First-principles calculations show that Ir preferentially occupies the central Ru(1) site of the Ru_3O_{12} trimer. This site-selective substitution disrupts the intratrimer interactions and reduces the magnetic connectivity of neighboring Ru(2) ions, effectively releasing them as paramagnetic $S = 1$ moments. Monte Carlo and Landau–Lifshitz–Gilbert spin-dynamics simulations further reproduce the key features of the magnetic sus-

ceptibility in the Ir-doped system. This work demonstrates how targeted substitution at electronically inactive sites can selectively tune magnetic properties and establish cluster-based oxides as the archetypal platform for engineering coexisting ordered and paramagnetic degrees of freedom.

ACKNOWLEDGEMENTS

G.C. acknowledges the support by the U.S. National Science Foundation via Grant No. DMR 2204811. X.H. and T.T.T thank the Arnold and Mabel Beckman Foundation, the NSF award NSF-DMR-2338014, and the Camille Henry Dreyfus Foundation. This research used resources at the High Flux Isotope Reactor and Spallation Neutron Sources, DOE Office of Science User Facilities operated by the Oak Ridge National Laboratory. The beam time was allocated to CORELLI on Proposal No. IPTS-34609 and VERITAS on Proposal No. IPTS-33477. ORNL is managed by UT-Battelle, LLC, under Contract No. DE-AC0500OR22725 for the U.S. Department of Energy. The U.S. Government retains and the publisher, by accepting the article for publication, acknowledges that the U.S. Government retains a nonexclusive, paid-up, irrevocable, worldwide license to publish or reproduce the published form of this manuscript, or allow others to do so, for the U.S. Government purposes. The Department of Energy will provide public access to these results of federally sponsored research in accordance with the DOE Public Access Plan.

DATA AVAILABILITY

The data that support the findings of this article are not publicly available upon publication because it is not technically feasible and/or the cost of preparing, depositing, and hosting the data would be prohibitive within the terms of this research project. The data are available from the authors upon reasonable request

Appendix A: Magnetic Structure Refinement

The magnetic structure of Ir-doped $\text{Ba}_4\text{Ru}_3\text{O}_{10}$ is determined using neutron diffraction measurements on the VERITAS triple-axis spectrometer at the High Flux Isotope Reactor. A series of rocking scans were collected at accessible Bragg positions both below ($T = 5$ K) and above ($T = 100$ K) the magnetic transition ($T_N = 84.0(1)$ K). The resulting scans were fitted with Gaussian profiles to extract integrated intensities with proper correction of instrument resolution in the triple-axis mode of the spectrometer. The magnetic scattering intensity was obtained by subtracting the high- T intensity from the corresponding low- T value. The list of extracted magnetic peaks, as listed in Table I, formed the experimental observables for the magnetic structure determination.

The intensities at $T = 100$ K were used to refine the nuclear structure and obtain the scale factor for the low- T data where Bragg intensities contain both magnetic and nuclear contribution. The refinement using the FullProf [41] suite included the thermal displacement parameters, scale factors, and extinction corrections. These parameters were then fixed for all subsequent magnetic refinements to ensure consistency across models.

For the propagation vector $\mathbf{k} = (0, 0, 0)$, symmetry analysis using the MAXMAGN tool [32] on the Bilbao Crystallographic Server [33–35] identifies eight symmetry-allowed magnetic space groups (MSGs) that are compatible with the crystal structure of $\text{Ba}_4\text{Ru}_3\text{O}_{10}$. For each MSG, the IRrep utility in FullProf was used to generate the irreducible representations (IRrep) and symmetry-allowed magnetic basis vectors for the crystallographically distinct Ru(1) and Ru(2) sites. The analysis yields four IRreps for Ru(1): Γ_1 , Γ_3 , Γ_5 , and Γ_7 , and eight IRreps for Ru(2): Γ_1 , Γ_2 , Γ_3 , Γ_4 , Γ_5 , Γ_6 , Γ_7 , and Γ_8 . These basis vectors were then matched to each MSG to form symmetry-consistent magnetic configurations. Each magnetic model was implemented in FullProf [41] and refined against the experimental magnetic intensities.

\mathbf{q}	F_{calc}^2	F_{obs}^2	\mathbf{q}	F_{calc}^2	F_{obs}^2
(0 0 $\bar{2}$)	19.21	22(5)	(1 3 $\bar{1}$)	2.27	2.6(7)
(0 4 2)	6.21	4.4(8)	($\bar{1}$ $\bar{3}$ $\bar{1}$)	2.27	1.9(5)
(0 4 $\bar{2}$)	6.21	5.5(8)	($\bar{1}$ $\bar{3}$ 1)	2.27	0.8(7)
(0 $\bar{4}$ $\bar{2}$)	6.21	4.2(9)	($\bar{1}$ $\bar{5}$ 0)	1.72	0.0(0)
($\bar{1}$ 3 0)	2.79	0.0(0)	($\bar{1}$ 1 0)	1.51	1.1(6)
(1 3 0)	2.79	2.5(5)	(1 $\bar{1}$ 0)	1.51	0.0(0)
($\bar{1}$ $\bar{3}$ 0)	2.79	0.0(0)	($\bar{1}$ $\bar{1}$ 0)	1.51	1.5(3)
($\bar{1}$ 3 $\bar{1}$)	2.27	1.1(6)	($\bar{1}$ $\bar{7}$ 0)	0.21	0.0(0)
(1 3 1)	2.27	1.0(5)	(0 4 $\bar{3}$)	0.03	0.6(5)

TABLE I. Calculated and observed magnetic structure factors at selected Bragg reflections, sorted in descending order of magnetic intensity.

#	Magnetic Spacegroup	Associated IRrep		
		Ru(1)	Ru(2)	χ^2/GOF
1	$\text{Cm}'c'a'$	–	$2\Gamma_2$	10.75
2	$\text{Cm}'ca'$	$2\Gamma_5$	$2\Gamma_5$	7.98
3	$\text{Cmc}'a'$	$1\Gamma_7$	$1\Gamma_7$	6.25
4	$\text{Cm}'c'a$	$2\Gamma_2$	$2\Gamma_3$	12.13
5	Cmca'	–	$1\Gamma_1$	11.26
6	$\text{Cmc}'a$	–	$1\Gamma_6$	0.89
7	$\text{Cm}'ca$	–	$2\Gamma_8$	3.57
8	Cmca	$1\Gamma_1$	$1\Gamma_4$	11.95

TABLE II. Candidate magnetic space groups (MSGs) and associated irreducible representations (IRreps) for the Ru(1) and Ru(2) sites. A dash indicates the absence of moment on that site.

The magnetic form factor of available Ru^{1+} [42] was used. The quality of each refinement was assessed by the goodness of fit χ^2 which is reported in Table II.

Appendix B: First-Principles Calculations

The electronic structure calculation was performed using the QUANTUM ESPRESSO (QE) package [43]. The exchange–correlation potential was treated within the Generalized Gradient Approximation (GGA) using the Perdew–Burke–Ernzerhof (PBE) functional [44]. On-site Coulomb interactions in the Ru $4d$ manifold were included via the GGA+U approach [45] ($U = 2.5$ eV). Projector-augmented wave (PAW) pseudo-potentials for Ba, Ru, Ir, and O were taken from the PSLIBRARY v.1.0.0 set [46]. Self-consistent calculations employed a $6 \times 3 \times 3$ k -point mesh in the irreducible Brillouin zone for both pristine and Ir-doped structures, with plane-wave kinetic-energy cutoffs of 52.1 eV for the wavefunctions and 469.1 eV for the charge density. Spin-density maps were computed using the QE post-processing module PP.X. Projected atomic charges and the density of energy were obtained using LOBSTER [47, 48]. Table III lists the energies from the DFT calculations which reveal that the most stable configuration with Ir-substitution is where it resides at the site in the middle of the trimer.

Sample	Total Energy (Ry/cell)	Rel. Energy (eV/cell)	Form. Energy (eV/cell)
100 K	-13829.32	3939.71	-2.99
Ir-Mid	-14119.09	0.00	-1.55
Ir-Edge	-14119.08	0.15	-1.40

TABLE III. Total, relative, and formation energies from first-principles calculations for undoped and Ir-doped $\text{Ba}_4\text{Ru}_3\text{O}_{10}$ configurations. The Ir-Mid configuration is the most stable among the doped variants.

Appendix C: Spin-Dynamics and Monte Carlo Simulations

We employed Monte Carlo (MC) and Landau–Lifshitz–Gilbert (LLG) spin-dynamics simulations to determine the magnetic ground state and finite-temperature magnetic response. The LLG calculations were performed using the SUNNY package [37]. Each Ru(2) ion is treated as an $S = 1$ moment with an onsite single-ion anisotropy term and a set of exchange interactions defined on the Ru₃O₁₂ trimer network. The Hamiltonian (\mathcal{H}) is given by

$$\begin{aligned} \mathcal{H} = & \sum_{\langle ij \rangle \in \text{trimer}} J_{\text{trimer}} \mathbf{S}_i \cdot \mathbf{S}_j + \sum_{\langle ij \rangle \in \text{chain}} J_{\text{chain}} \mathbf{S}_i \cdot \mathbf{S}_j \\ & + \sum_{\langle ij \rangle \in \text{plane}} J_{\text{plane}} \mathbf{S}_i \cdot \mathbf{S}_j - D \sum_i (S_i^x)^2. \end{aligned} \quad (\text{C1})$$

with double counting bond pairs between atom i and j omitted. The positive sign of the exchange interaction J indicates an antiferromagnetic coupling whereas for the single ion term D provides easy axis alignment along the a -axis.

Reference	Method	^a x	^b J_{trimer}	^b J_{chain}	^b J_{plane}	^b D
This work	LLG & MC	0%	11.5	4.5	0.5	2
		8%	11.5	4.5	0.5	2
Igarashi 2015 [39]	Dimer(χ fit)	0%	14.6	^c 5.2	-	-
		7%	14.3	^c 5.2	-	-
		10%	14.1	^c 5.1	-	-
		17%	13.8	^c 5.0	-	-
Sannigrahi	INS(spin wave)	0%	11.5	4.5	0.5	2.9
2021 [15]	DFT(GGA)	0%	14.9	3.7	1.1	-
	DFT(GGA+U)	0%	11.4	1.3	0.48	-
Radtke	DFT(GGA)	0%	14.8	3.7	1.1	-
2013 [49]	DFT(GGA+U)	0%	11.4	1.29	0.43	-

^a x denotes the Ir concentration in Ba₄(Ru_{1-x}Ir_x)₃O₁₀.

^b All interaction parameters are given in the units of meV and are normalized such that $\mathbf{S} \cdot \mathbf{S} = S(S+1)$.

^c For the dimer model of Ref. [39], only the combined inter-trimer exchange ($J_{\text{chain}} + J_{\text{trimer}}$) is reported.

TABLE IV. Comparison of magnetic interaction parameters from the literature and the effective values used in our Landau–Lifshitz–Gilbert (LLG) and Monte Carlo (MC) simulations. The ratios of the exchange couplings in our model are chosen to be broadly consistent with those inferred in Ref. [39] while on the scale of Ref. [15]. The simulation parameters refer to the bond-paired exchange interactions. The doped system is distinguished from the parent compound by the fraction of paramagnetic sites f_{PM} , which encodes the effect of Ir substitution. Thus, assuming the underlying exchange interaction strengths remain unchanged far from Ir-substituted sites. The resulting Néel temperature and magnetic susceptibility arise as observables of the model, and alternative parameter sets may equally well reproduce these quantities.

The three exchange terms in Eq. C1 correspond to the magnetic pathways shown in Fig. 1. The dominant coupling, J_{trimer} , acts along the face-sharing RuO₆ octahedra that form the Ru₃O₁₂ trimer units. This interaction connects the three Ru(2) sites within each trimer and is responsible for the zigzag AFM ordering. The second term, J_{chain} , couples neighboring trimers and generates one-dimensional magnetic chains that propagate through the structure. The final term, J_{plane} , links trimers across the plane. The chain- and plane- interactions are necessary for establishing the three-dimensional long-range order. The non-magnetic Ru(1) sites are omitted. Ir substitution is incorporated by diluting the exchange network. The Ru–Ru trimer bond is removed for the trimer consisting of Ir atom in the middle site. Whenever such a bond-interaction is deleted, both connected Ru sites are classified as *paramagnetic*. These sites retain $S = 1$ moments but all exchange couplings to them (trimer, chain, and plane bonds) are removed. This procedure generates an inhomogeneous system in which weakly interacting paramagnetic spins coexist with an AFM ordered backbone. Effectively, this dilution procedure produces a fraction of paramagnetic Ru sites given by $f_{\text{PM}} \approx 0.24 \times 2/3 = 0.16$, once the presence of the nonmagnetic Ru(1) sites is taken into account. This value follows from the assumption that each substituted Ir atom occupies the central Ru(1) site and releases two Ru(2) moments, so an Ir concentration of $x = 0.08$ yields $f_{\text{PM}} = 0.16$ free Ru spins.

The magnetic ground state is obtained by randomizing all spins, followed by a finite-temperature Langevin relaxation of the LLG equation. For the MC simulations, a replica exchange procedure is employed over the temperature range of interest [50]. At each temperature, the system is equilibrated using Langevin dynamics or Monte Carlo Metropolis sweep. These procedures both converge to a zigzag AFM configuration on the Ru(2) sites, yielding a moment configuration consistent with the neutron-refined structure at lowest temperature. The calculated magnetic order parameter is obtained from the integrated static structure factor $I_{\text{tot}}(T) = \sum_{\mathbf{Q}} S(\mathbf{Q})$ around the (110) magnetic Bragg position.

The exchange parameters in our model are obtained starting with the interaction strengths derived from inelastic neutron scattering reported in Ref. [15] cross validating that the simulated ordering temperature reproduces the experimental value $T_{\text{N}} \approx 105$ K for pure BRO. The T dependence of the order parameter is plotted in Fig. 3(d) measured at HB1A and compared with MC simulation. The single-ion anisotropy is lowered slightly to better model the transition temperature while reducing the Ising-like temperature-dependence obtained from the original parameters. It is noted that for both the LLG and MC simulations, the parameters correspond to an effective spin dipole Hamiltonian. The full set of interaction parameters used in these simulations is summarized in Table IV. The simulation with a paramagnetic-site fraction $f_{\text{PM}} \approx 0.16$ with the same exchange interactions

as the parent-compound parameters closely tracks the experimental order-parameter curve and yields a transition temperature of $T_N \approx 84$ K, in agreement with neutron diffraction. In contrast, the undiluted simulation ($f_{PM} = 0$) using the same exchange parameters for the parent compound reproduces the higher transition temperature of $T_N \approx 105$ K reported in Ref. [13]. This comparison demonstrates that the dilution of exchange network contribute to the suppression of T_N in the Ir-doped system.

Directional susceptibilities $\chi_a(T)$, $\chi_b(T)$, and $\chi_c(T)$ were calculated from the magnetization fluctuations. At each temperature, the system was equilibrated for 100,000 Langevin steps and sampled for an additional

5,000 steps to obtain statistically converged susceptibility values. The calculated susceptibilities are compared with experimental data in Fig. 2. These results are validated using spin Heisenberg Monte Carlo simulation with parallel tempering; sweeps of 30,000 for equilibration and 20,000 for sampling are used, extracting the same susceptibilities and order parameter. The LLG and MC simulations reproduce the qualitative behavior of the susceptibility.

We have verified that the LLG spin-dynamics simulations performed using SUNNY yield temperature dependencies of the magnetic order parameter and susceptibility that are qualitatively consistent with the MC results. For clarity, only the MC data are presented.

-
- [1] C. Dussarrat, F. Grasset, R. Bontchevb, and J. Darrriet, Crystal structures and magnetic properties of $\text{Ba}_4\text{Ru}_3\text{O}_{10}$ and $\text{Ba}_5\text{Ru}_3\text{O}_{12}$, *J. Alloys Compd.* **233**, 15 (1996).
- [2] P. C. Donohue, L. Katz, and R. Ward, The Crystal Structure of Barium Ruthenium Oxide and Related Compounds, *Inorg. Chem.* **4**, 306 (1965).
- [3] G. Gebreyesus, P. Ngabonziza, J. Nagura, N. Seriani, O. Akin-Ojo, and R. M. Martin, Electronic structure and magnetism of the triple-layered ruthenate $\text{Sr}_4\text{Ru}_3\text{O}_{10}$, *Phys. Rev. B* **105**, 165119 (2022).
- [4] R. Gupta, R. Rawat, and A. K. Pramanik, Electronic properties in itinerant ferromagnet $\text{SrRu}_{1-x}\text{Ti}_x\text{O}_3$, *J. Phys.: Condens. Matter* **32**, 285502 (2020).
- [5] L. T. Nguyen and R. Cava, A spin glass state in $\text{Ba}_3\text{TiRu}_2\text{O}_9$, *J. Magn. Mater.* **476**, 334 (2019).
- [6] Y. Maeno, H. Hashimoto, K. Yoshida, S. Nishizaki, T. Fujita, J. G. Bednorz, and F. Lichtenberg, Superconductivity in a layered perovskite without copper, *Nature* **372**, 532 (1994).
- [7] A. P. Mackenzie and Y. Maeno, The superconductivity of Sr_2RuO_4 and the physics of spin-triplet pairing, *Rev. Mod. Phys.* **75**, 657 (2003).
- [8] C. Bergemann, A. P. Mackenzie, S. R. Julian, D. Forsythe, and E. Ohmichi, Quasi-two-dimensional Fermi liquid properties of the unconventional superconductor Sr_2RuO_4 , *Adv. Phys.* **52**, 639 (2003).
- [9] T. M. Rice and M. Sigrist, Sr_2RuO_4 : An electronic analogue of ^3He ?, *J. Phys. Condens. Matter* **7**, L643 (1995).
- [10] C. W. Hicks, D. O. Brodsky, E. A. Yelland, A. S. Gibbs, J. A. N. Bruin, M. E. Barber, S. D. Edkins, K. Nishimura, S. Yonezawa, Y. Maeno, and A. P. Mackenzie, Strong Increase of T_C of Sr_2RuO_4 Under Both Tensile and Compressive Strain, *Science* **344**, 283 (2014).
- [11] S. Yonezawa, T. Kajikawa, and Y. Maeno, First-Order Superconducting Transition of Sr_2RuO_4 , *Phys. Rev. Lett.* **110**, 077003 (2013).
- [12] C. Kallin, Chiral p-wave order in Sr_2RuO_4 , *Rep. Prog. Phys.* **75**, 042501 (2012).
- [13] Y. Klein, G. Rousse, F. Damay, F. Porcher, G. André, and I. Terasaki, Antiferromagnetic order and consequences on the transport properties of $\text{Ba}_4\text{Ru}_3\text{O}_{10}$, *Phys. Rev. B* **84**, 054439 (2011).
- [14] T. Igarashi, Y. Nogami, Y. Klein, G. Rousse, R. Okazaki, H. Taniguchi, Y. Yasui, and I. Terasaki, X-ray Crystal Structure Analysis and Ru Valence of $\text{Ba}_4\text{Ru}_3\text{O}_{10}$ Single Crystals, *J. Phys. Soc. Jpn.* **82**, 104603 (2013).
- [15] J. Sannigrahi, A. Paul, A. Banerjee, D. Khalyavin, A. D. Hillier, K. Yokoyama, A. K. Bera, M. R. Lees, I. Dasgupta, S. Majumdar, and D. T. Adroja, Orbital effects and Affleck–Haldane-type spin dimerization in $\text{Ba}_4\text{Ru}_3\text{O}_{10}$, *Phys. Rev. B* **103**, 144431 (2021).
- [16] S. Hayashida, H. Gretarsson, P. Puphal, M. Isobe, E. Goering, Y. Matsumoto, J. Nuss, H. Takagi, M. Hepting, and B. Keimer, Magnetic ground state of the dimer-based hexagonal perovskite $\text{Ba}_3\text{ZnRu}_2\text{O}_9$, *Phys. Rev. B* **111**, 104418 (2025).
- [17] S. V. Streltsov and D. I. Khomskii, Cluster Magnetism of $\text{Ba}_4\text{NbMn}_3\text{O}_{12}$: Localized Electrons or Molecular Orbitals?, *Jetp Lett.* **108**, 686 (2018).
- [18] A. Ali, H.-S. Kim, P. Yadav, S. Lee, D. Yoon, and S. Choi, Partial molecular orbitals in face-sharing $3d$ manganese trimer: Comparative studies on $\text{Ba}_4\text{TaMn}_3\text{O}_{12}$ and $\text{Ba}_4\text{NbMn}_3\text{O}_{12}$, *Phys. Rev. Research* **6**, 013231 (2024).
- [19] S. V. Streltsov and D. I. Khomskii, Covalent bonds against magnetism in transition metal compounds, *Proc. Natl. Acad. Sci. U.S.A.* **113**, 10491 (2016).
- [20] W. Miiller, M. Avdeev, Q. Zhou, A. J. Studer, B. J. Kennedy, G. J. Kearley, and C. D. Ling, Spin-gap opening accompanied by a strong magnetoelastic response in the $S = 1$ magnetic dimer system $\text{Ba}_3\text{BiRu}_2\text{O}_9$, *Phys. Rev. B* **84**, 220406 (2011).
- [21] I. Terasaki, T. Igarashi, T. Nagai, K. Tanabe, H. Taniguchi, T. Matsushita, N. Wada, A. Takata, T. Kida, M. Hagiwara, K. Kobayashi, H. Sagayama, R. Kumai, H. Nakao, and Y. Murakami, Absence of Magnetic Long Range Order in $\text{Ba}_3\text{ZnRu}_2\text{O}_9$: A Spin-Liquid Candidate in the $S = 3/2$ Dimer Lattice, *J. Phys. Soc. Jpn.* **86**, 033702 (2017).
- [22] M. S. Senn, A. M. Arevalo-Lopez, T. Saito, Y. Shimakawa, and J. Paul Attfield, Nonmagnetic spin-singlet dimer formation and coupling to the lattice in the 6H perovskite $\text{Ba}_3\text{CaRu}_2\text{O}_9$, *J. Phys.: Condens. Matter* **25**, 496008 (2013).
- [23] J. T. Rijssenbeek, R. Jin, Yu. Zadorozhny, Y. Liu, B. Batlogg, and R. J. Cava, Electrical and magnetic properties of the two crystallographic forms of BaRuO_3 , *Phys. Rev. B* **59**, 4561 (1999).

- [24] C.-Q. Jin, J.-S. Zhou, J. B. Goodenough, Q. Q. Liu, J. G. Zhao, L. X. Yang, Y. Yu, R. C. Yu, T. Katsura, A. Shatskiy, and E. Ito, High-pressure synthesis of the cubic perovskite BaRuO₃ and evolution of ferromagnetism in ARuO₃ (A = Ca, Sr, Ba) ruthenates, *Proc. Natl. Acad. Sci. U.S.A.* **105**, 7115 (2008).
- [25] Y. Doi, K. Matsuhira, and Y. Hinatsu, Crystal Structures and Magnetic Properties of 6H-Perovskites Ba₃MRu₂O₉ (M=Y, In, La, Sm, Eu, and Lu), *J. Solid State Chem.* **165**, 317 (2002).
- [26] S. V. Streltsov and D. I. Khomskii, Unconventional magnetism as a consequence of the charge disproportionation and the molecular orbital formation in Ba₄Ru₃O₁₀, *Phys. Rev. B* **86**, 064429 (2012).
- [27] T. Basu, F. Y. Wei, Q. Zhang, Y. Fang, and X. Ke, Complex magnetic structure in Ba₅Ru₃O₁₂ with isolated Ru₃O₁₂ trimer, *Phys. Rev. Materials* **4**, 114401 (2020).
- [28] Y. Shimoda, Y. Doi, M. Wakeshima, and Y. Hinatsu, Magnetic properties of quadruple perovskites Ba₄LnRu₃O₁₂ (Ln = La, Nd, Sm–Gd, Dy–Lu), *J. Solid State Chem.* **183**, 33 (2010).
- [29] E. C. Stoner, Ferromagnetism, *Rep. Prog. Phys.* **11**, 43 (1947).
- [30] G. Cao, H. Zheng, H. Zhao, Y. Ni, C. A. Pocs, Y. Zhang, F. Ye, C. Hoffmann, X. Wang, M. Lee, M. Hermele, and I. Kimchi, Quantum liquid from strange frustration in the trimer magnet Ba₄Ir₃O₁₀, *npj Quantum Mater.* **5**, 26 (2020).
- [31] F. Ye, Y. Liu, R. Whitfield, R. Osborn, and S. Rosenkranz, Implementation of cross correlation for energy discrimination on the time-of-flight spectrometer CORELLI, *J. Appl. Crystallogr.* **51**, 315 (2018).
- [32] J. Perez-Mato, S. Gallego, E. Tasci, L. Elcoro, G. De La Flor, and M. Aroyo, Symmetry-Based Computational Tools for Magnetic Crystallography, *Annu. Rev. Mater. Res.* **45**, 217 (2015).
- [33] M. I. Aroyo, J. M. Perez-Mato, C. Capillas, E. Kroumova, S. Ivantchev, G. Madariaga, A. Kirov, and H. Wondratschek, Bilbao Crystallographic Server: I. Databases and crystallographic computing programs, *Z. Kristallogr. NCS* **221**, 15 (2006).
- [34] M. I. Aroyo, A. Kirov, C. Capillas, J. M. Perez-Mato, and H. Wondratschek, Bilbao Crystallographic Server. II. Representations of crystallographic point groups and space groups, *Acta Crystallogr A, Found Crystallogr* **62**, 115 (2006).
- [35] M. Aroyo, J. Perez-Mato, D. Orobengoa, E. Tasci, G. De La Flor, and A. Kirov, Crystallography online: Bilbao crystallographic server, *Bulg. Chem. Commun.* **43**, 183 (2011).
- [36] H. Matsuura and K. Miyake, Effect of Spin–Orbit Interaction on (4d)³- and (5d)³-Based Transition-Metal Oxides, *J. Phys. Soc. Jpn.* **82**, 073703 (2013).
- [37] D. Dahlbom, H. Zhang, C. Miles, S. Quinn, A. Niraula, B. Thipe, M. Wilson, S. Matin, H. Mankad, S. Hahn, D. Pajeroski, S. Johnston, Z. Wang, H. Lane, Y. W. Li, X. Bai, M. Mourigal, C. D. Batista, and K. Barros, Sunny.jl: A Julia Package for Spin Dynamics, *J. Open Source Softw.* **10**, 8138 (2025).
- [38] R. D. Shannon, Revised effective ionic radii and systematic studies of interatomic distances in halides and chalcogenides, *Acta Cryst A* **32**, 751 (1976).
- [39] T. Igarashi, R. Okazaki, H. Taniguchi, Y. Yasui, and I. Terasaki, Effects of the Ir Impurity on the Thermodynamic and Transport Properties of Ba₄Ru₃O₁₀, *J. Phys. Soc. Jpn.* **84**, 094601 (2015).
- [40] G. Cao, H. Zhao, A. Bond, T. R. Cao, G. Schebel, A. Quane, Y. Ni, Y. Zhang, L. Wall, R. Nandkishore, P. Schlottmann, and F. Ye, Hidden Density-Wave Instability in the Trimer Ruthenate Ba₄Ru₃O₁₀ (2026).
- [41] J. Rodríguez-Carvajal, Recent advances in magnetic structure determination by neutron powder diffraction, *Physica B Condens. Matter.* **192**, 55 (1993).
- [42] E. Prince, H. Fuess, Th. Hahn, H. Wondratschek, U. Müller, U. Shmueli, E. Prince, A. Authier, V. Kopský, D. B. Litvin, M. G. Rossmann, E. Arnold, S. Hall, and B. McMahan, eds., *International Tables for Crystallography: Mathematical, Physical and Chemical Tables*, 1st ed., International Tables for Crystallography, Vol. C (International Union of Crystallography, Chester, England, 2006).
- [43] P. Giannozzi, S. Baroni, N. Bonini, M. Calandra, R. Car, C. Cavazzoni, D. Ceresoli, G. L. Chiarotti, M. Cococcioni, I. Dabo, A. Dal Corso, S. De Gironcoli, S. Fabris, G. Fratesi, R. Gebauer, U. Gerstmann, C. Gougoussis, A. Kokalj, M. Lazzeri, L. Martin-Samos, N. Marzari, F. Mauri, R. Mazzarello, S. Paolini, A. Pasquarello, L. Paulatto, C. Sbraccia, S. Scandolo, G. Sclauzero, A. P. Seitsonen, A. Smogunov, P. Umari, and R. M. Wentzcovitch, QUANTUM ESPRESSO: A modular and open-source software project for quantum simulations of materials, *J. Phys.: Condens. Matter* **21**, 395502 (2009).
- [44] J. P. Perdew, A. Ruzsinszky, G. I. Csonka, O. A. Vydrov, G. E. Scuseria, L. A. Constantin, X. Zhou, and K. Burke, Restoring the Density-Gradient Expansion for Exchange in Solids and Surfaces, *Phys. Rev. Lett.* **100**, 136406 (2008).
- [45] L. Wang, T. Maxisch, and G. Ceder, Oxidation energies of transition metal oxides within the GGA + U framework, *Phys. Rev. B* **73**, 195107 (2006).
- [46] A. Dal Corso, Pseudopotentials periodic table: From H to Pu, *Comput. Mater. Sci.* **95**, 337 (2014).
- [47] S. Maintz, V. L. Deringer, A. L. Tchougréeff, and R. Dronskowski, LOBSTER: A tool to extract chemical bonding from plane-wave based DFT, *J. Comput. Chem.* **37**, 1030 (2016).
- [48] R. Nelson, C. Ertural, J. George, V. L. Deringer, G. Hautier, and R. Dronskowski, LOBSTER: Local orbital projections, atomic charges, and chemical-bonding analysis from PROJECTOR-AUGMENTED-WAVE-BASED density-functional theory, *J. Comput. Chem.* **41**, 1931 (2020).
- [49] G. Radtke, A. Saúl, Y. Klein, and G. Rousse, Magnetism of Ba₄Ru₃O₁₀ revealed by density functional calculations: Structural trimers behaving as coupled magnetic dimers, *Phys. Rev. B* **87**, 054436 (2013).
- [50] Z. Morgan and F. Ye, Toward Discord: Code for Simulating Continuous Spin Systems, *JOM* **74**, 2338 (2022).